LA-6407

UC-37

Issued: November 1976

A 256-line, 2.8-ms Field Duration TV Camera

by

George J. Yates
Bruce W. Noel

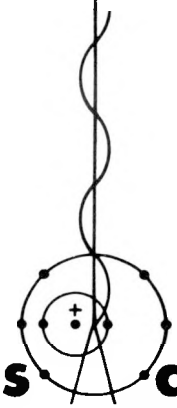

los alamos
scientific laboratory
of the University of California
LOS ALAMOS, NEW MEXICO 87545

UNITED STATES
ENERGY RESEARCH AND DEVELOPMENT ADMINISTRATION
CONTRACT W-7405-ENG. 36

Printed in the United States of America. Available from
National Technical Information Service
U.S. Department of Commerce
5285 Port Royal Road
Springfield, VA 22161
Price: Printed Copy $3.50 Microfiche $3.00

A 256-LINE, 2.8-ms FIELD DURATION TV CAMERA

by

George J. Yates and Bruce W. Noel

ABSTRACT

A prototype 256-line, 2.8-ms field duration television camera was designed, built, and successfully field tested by the Los Alamos Scientific Laboratory (LASL). It used an FPS vidicon tube to maintain good resolution while achieving the short field time. Additional features included 9.5 μs active line time out of 10 μs total, 10-V peak-to-peak video output into 50 Ω, a dynamic range between 64 and 128, and remotely resettable sweeps.

This report includes details of design philosophy regarding the selection of the FPS vidicon, the parameters that affect the choice of the target material, the electronic design, and the calibration procedures.

I. INTRODUCTION

For several years we have used a modified extended-dynamic-range (EDR) version of an MTI (Maryland Telecommunications, Inc.) VC-20 magnetically deflected and focused vidicon TV camera[1] for the data acquisition in downhole neutron Pinex experiments. The demands imposed by a new close-in Pinex scheme[2] require <3-ms field readout times, in contrast to the 8.33 ms of the EDR camera, and constrain the minimum acceptable resolution to >200 scan lines with limiting horizontal resolution >100 line pairs per scan line.

Electrostatically deflected vidicon cameras were ruled out for our application. Such cameras, normally electrostatically focused, inherently produce resolution inferior to that achieved by magnetically focused systems.

An evaluation of existing electromagnetic-deflection cameras showed that the modifications needed to achieve high scan rates with conventional rastering are impractical because of excessive current, voltage, and power levels. This evaluation is summarized in Appendix A. Note that such unconventional electromagnetic camera designs as those utilizing zig-zag scanning and/or smaller than nominal raster sizes are not necessarily ruled out.

Given the inferior resolution of electrostatic-deflection cameras, and given the difficult design problems inherent in using electromagnetic-deflection cameras in an ultrafast-scan mode, we chose to approach the problem by designing a new camera using a tube without those limitations. A prototype version of this camera was fielded successfully in a recent underground test.

II. DESIGNING THE CAMERA

A. Choosing the Vidicon

Because both good resolution and fast deflection are essential, we chose a General Electric (GE) hybrid mixed-field vidicon that uses electrostatic deflection and electromagnetic focus. Focus projection and scanning (FPS) are accomplished simultaneously because both fields are superimposed in the same volume. FPS vidicons use an external solenoidal focus coil, an internal cylindrical or conical electrostatic-deflection assembly (called a

deflectron), and demagnifying electron optics to produce a small electron-beam spot size with high electron density in the beam. From the electron-optical standpoint, the system behaves like a scanning lens that moves in a plane parallel to the target, while projecting onto the target an image of either the beam-defining aperture or the actual beam crossover, depending on the FPS design. A comprehensive analysis of the electron-optic principles of FPS vidicons is contained in the literature.[3-5]

Of several designs developed by GE, all achieve varying degrees of demagnification of the electron beam. Figure 1 illustrates the basic features of two of the FPS tube designs. In the design at the top, the electron beam leaves the cathode (K) through the object aperture (A) and traverses an object drift space (a) before entering the FPS cavity (D). The cavity is surrounded by a cylindrical deflectron (E) and is terminated by the target mesh (M). The deflectron is surrounded by an external focus coil (F). When appropriate electromagnetic fields are applied, the cavity will focus an image of (A) on the target (P) within the image distance (b). System magnification[3] is dependent upon the relationship between the object space (a) and the image distance (b). Magnification is unity for a = b, but for a > b the system achieves demagnification. The design at the bottom incorporates a feature called "internal-focus projection."[4] In this design, which minimizes shading due to beam-landing error, the electron

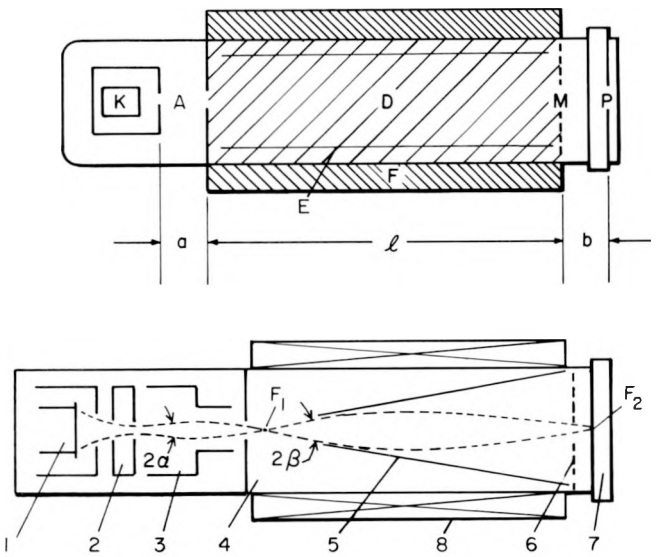

Fig. 1.
Cross-sections of two types of FPS vidicon.[3,4]

beam leaves the cathode (1) through the object aperture (2) and enters the electrostatic prefocus lens (3) at diverging angle 2α. The lens focuses (reconverges) the beam inside the FPS cavity (4) at angle 2β ($2\beta > 2\alpha$) such that a real image of the aperture (F_1) (F_1 < object aperture) is formed. In this figure, (5) is the conical deflectron, (6) is the terminating mesh, and (8) is the external focus coil. Again, when appropriate electromagnetic fields are applied, the FPS cavity refocuses F_1 at unity magnification of F_1 into the actual scanning spot (F_2) at the target (7). For system demagnification, the prefocus electrostatic lens projects a real image F_1 of the beam aperture (2) into the FPS cavity (4) such that F_1 is smaller in diameter than the aperture.

The importance of demagnification is twofold. First, if the read beam can be concentrated in a smaller area, the electron-optic resolution is improved because more beam diameters can be resolved or "fitted" along a given segment of the vidicon target. Vidicon spatial frequency response is proportional to beam diameter because more closely spaced adjacent black-and-white line pairs can be better resolved with decreasing beam diameters. Second, if all the electrons in the read beam can be concentrated in a smaller area, the electron density will increase. Therefore, the number of electrons available to neutralize stored charges at a given target site will be increased by the reciprocal of the square of the ratio of new and old diameters.

The two demagnification effects are summarized in the formula for the relative beam densities, $J_2 = J_1/M^2$, where J_2 is the magnified beam current density, J_1 is the unity magnification (non-FPS) density, and M is the magnification (ratio of beam diameters). Because a typical beam-magnification value in an FPS tube approaches 0.6, an electron-beam density approaching three times that of conventional vidicons can be expected. This high-density beam provides the designer with a powerful tool. Theoretically, the beam scan speed (a function of horizontal scan rate) can be increased to approximately three times conventional rates and can still produce essentially the same signal current from a given charge site on the target. Furthermore, at conventional scan rates, assuming reciprocity and also adequate charge storage on the target, signal currents from a given site could approach three times the magnitude achieved with conventional vidicons.

A recent GE design known as the "printed on wall" (POW) deflectron FPS is described in Ref. 5. In this type of FPS, the deflection assembly is evaporated

onto the glass wall of the tube, a feature reported to minimize microphonic noise and increase tube ruggedness. The new design also reportedly has 60-70% fewer internal tube parts than do conventional magnetic tubes.

Table I gives experimental data, and attendant approximations of read-beam currents, diameters, and resultant resolution, for two different FPS vidicons and for two conventional electromagnetic vidicons.[3-10]

B. Target Selection

The second design step (after FPS vidicon selection) involved selecting a suitable target. The choice was between Sb_2S_3 photoconductive and silicon-diode matrix targets. We favored a silicon vidicon because its absolute spectral responsivity is greater than that of Sb_2S_3 vidicons over the visible spectrum.[11,12] Figure 2 shows the comparison. Silicon manufacturing technology has resulted in high-quality materials with few trapping centers. The relative absence of traps increases silicon's quantum efficiency (number of carriers generated per incident photon) to nearly unity throughout the visible range. The response falls off in the ultraviolet because of absorption in the glass faceplate and in the near infrared because of the rapidly decreasing absorption coefficient near the band edge at 1.1 μm.

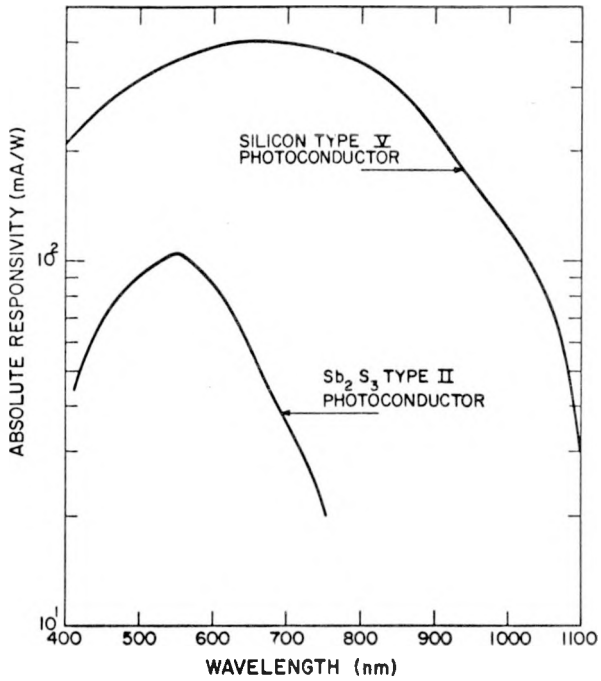

Fig. 2.
Absolute responsivities of RCA 8573A Sb_2S_3 photoconductor and RCA 4532A silicon-diode matrix vidicons over entire visible spectrum. Curves redrawn from RCA data sheets.

TABLE I

COMPARATIVE RESOLUTION CHARACTERISTICS OF TWO TYPICAL CONVENTIONAL VIDICONS (FOCUSED AND DEFLECTED ELECTROMAGNETICALLY) AND OF TWO DIFFERENT FPS VIDICONS

Vidicon Type	Apparent Beam Diameter (μm)	Limiting Spatial Resolution at the Target (lp/mm)	Beam Current Available at the Target (μA)	Amplitude Response at 400 TV Lines (% of dc Response)
GE 8573A	10-12 (6)	15-25 (3,8)	0.5-0.75 (5,8)	40-50 (3,8)
RCA 8507		15-25 (7)	0.2-0.6 (7)	30-40 (7)
Original FPS GE Z7873S	7-10 (3,4)	33-50 (3,4)	0.5-1 (3,9)	78-85 (3,9)
POW FPS GE Z7801	6-7 (5,6)	80-90 (5,10)	1-2 (5)	85-90 (5,10)

Note: The numbers in parentheses refer to text references.

Data taken earlier[1] using an EDR camera and vidicons of several different target materials were compared with the manufacturer's curves. The data were taken in two steps: (1) with a broad-spectral-range light source (pulsed General Radio Type 1538-A Strobotac), and (2) with the same source, but using a blue transmission filter that restricted the light range to between about 375 nm and 475 nm. The transmission characteristics of the blue filter, a Corning CS5-61, are shown in Fig. 3.

Both vidicons were exposed to the same input radiant flux. The critical vidicon parameters were adjusted for optimum tube performance in each case. Figure 4 shows the observed responses. The waveforms are of a single EDR-camera horizontal scan line measured at the preamplifier output. The source pattern was a circular spot of diffused light with a wide vertical black bar through the middle.

A Kodak Wratten N.D. 0.6 neutral-density (ND) filter was placed over the right-hand half of the source pattern so that the transmitted light intensity had two calibrated peaks (maximums). The intensity of the light transmitted through the unfiltered part of the pattern is about twice that transmitted through the filtered part. This calibration was performed so that we could recognize when the vidicons were operating on the linear portion of their respective transfer curves. The smaller amplitude signals, from the filtered portion of the scene, are approximately half as large as their unfiltered counterparts, indicating that the camera indeed was operating linearly.

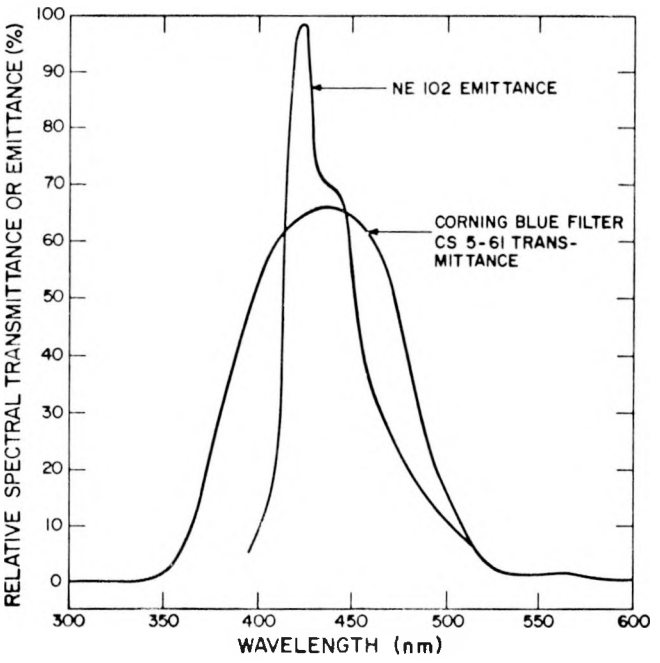

Fig. 3.
Transmittance characteristics of Corning CS5-61 blue glass transmission filter, and emittance characteristics of NE-102 radiation-to-light converter.

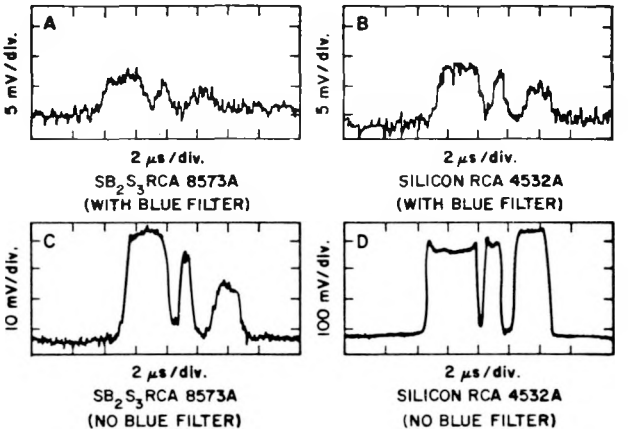

Fig. 4.
Observed comparative responsivities of Sb_2S_3 and silicon vidicons as redrawn from oscilloscope photographs.

The response in this spectral range (375-475 nm) is important because of the spectral output in the blue of the NE-102 radiation-to-light converter[13] used in Pinex experiments (Fig. 3). The observed responses in the blue only, and over the entire spectrum of the light source, are about 40% higher for the silicon vidicon than for the Sb_2S_3 vidicon (Fig. 4).

The lower dark current of silicon was also attractive. Silicon dark currents are typically 7 nA, whereas Sb_2S_3 dark currents of 200 nA are common with large target voltages. The lower dark current improves pickup tube dynamic range because beam current is not wasted in discharging the dark current. Tube shading also is minimized at lower dark currents.

Finally, and most important, the predicted response time of silicon[14] ("soak" time, or the time required for image buildup after input radiant flux is applied) is shorter than the observed response time for Sb_2S_3.[1] The typical Sb_2S_3 soak time requirement of about 1 ms would use too much of the limited readout time available in close-in Pinex experiments.

Figure 5 shows experimental Sb_2S_3 soak data as a function of target voltage. Figure 6 shows the effect

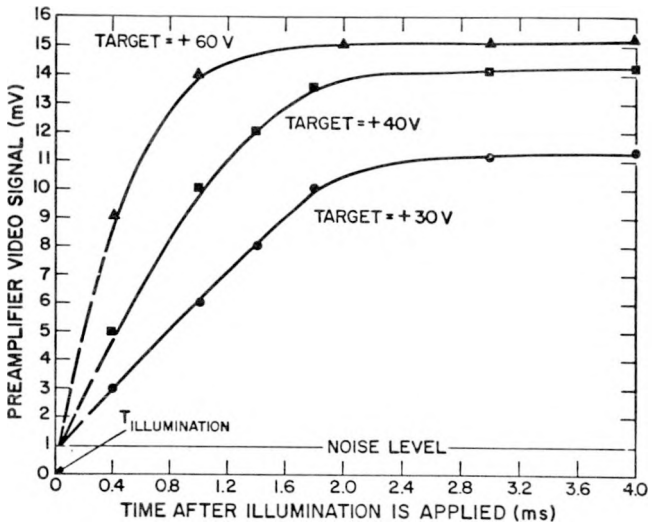

Fig. 5.
Observed soak characteristics of 8573A Sb_2S_3 vidicons as a function of increasing target voltage.

of varying the physical location of the incident light pulse on the vidicon target. Because beam arrival at the site is a function of the sweep, varying the image location effectively varies the time period from illumination to beam interrogation of the resultant stored charge. The observed soak status (degree of completion of light-to-charge transfer) of 8573A Sb_2S_3 vidicons is a function of the time period between application of the incident flux and the beginning of interrogation by the read beam. We

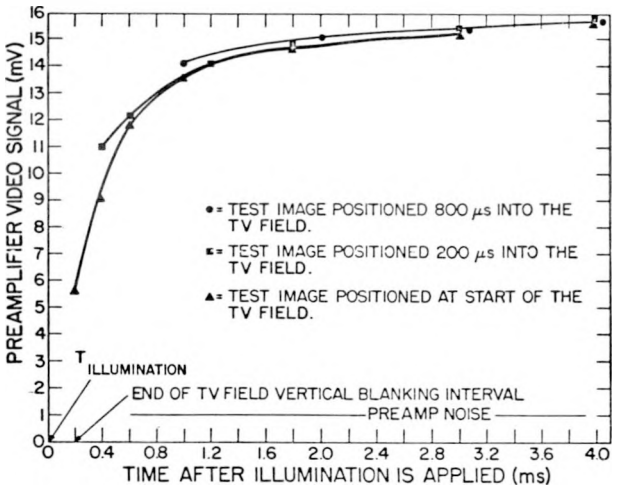

Fig. 6.
Observed soak status of 8573A Sb_2S_3 vidicons as a function of varying image location on the target.

varied the physical position of the light source (a uniformly illuminated low-spatial-frequency content pattern of equally spaced black-and-white vertical bars, an ND filter, appropriate diffusers, and an EG&G Model No. 1 pulsed optoliner). This was done so that the location of the formed image on the vidicon target would be so positioned that different numbers of horizontal scan lines had to be swept out before the optical data were encountered. A theoretical analysis of the soak time is included in Appendix B.

C. Electronics

To meet field test schedules, the prototype FPS camera was to be based as much as possible on the existing EDR camera head and camera control unit (CCU) chassis. Preliminary evaluation showed that virtually none of the existing circuitry could be used. Synchronization (sync) and timing circuits were unusable because the new camera required different scan formats; existing sweep circuits designed for magnetic rather than electrostatic deflection were not usable; and FPS vidicon operating voltages and current requirements are so different from normal vidicon values that most existing power supplies provided either incorrect voltages or inadequate currents. In addition, although the video amplifier bandwidths were inadequate, they were retained in the prototype both because of time limitations and because it is relatively easy to account for their bandwidth-limiting effects in postdesign performance analysis.

The EDR chassis was reduced in width by one-third, and the unusable existing circuit modules were replaced with new designs. The VC-20 head required complete redesign to accommodate extensive shielding needed to protect the sensitive components (vidicon and preamp) from device-generated radiation in the close-in experiment. Figure 7 is a drawing of the camera head with the cover removed to show the locations of the various components. Figures 8 and 9 are photographs of the head, and of the head and modified CCU, respectively. The CCU door in Fig. 9 is open, showing the modular layout and a redesigned module (on the extender board) that contains the sweep and cathode-blanking circuits. The motor-driven potentiometers used to control various camera parameters remotely are also shown.

Because this camera was to be located approximately half as far from the device in the experiment

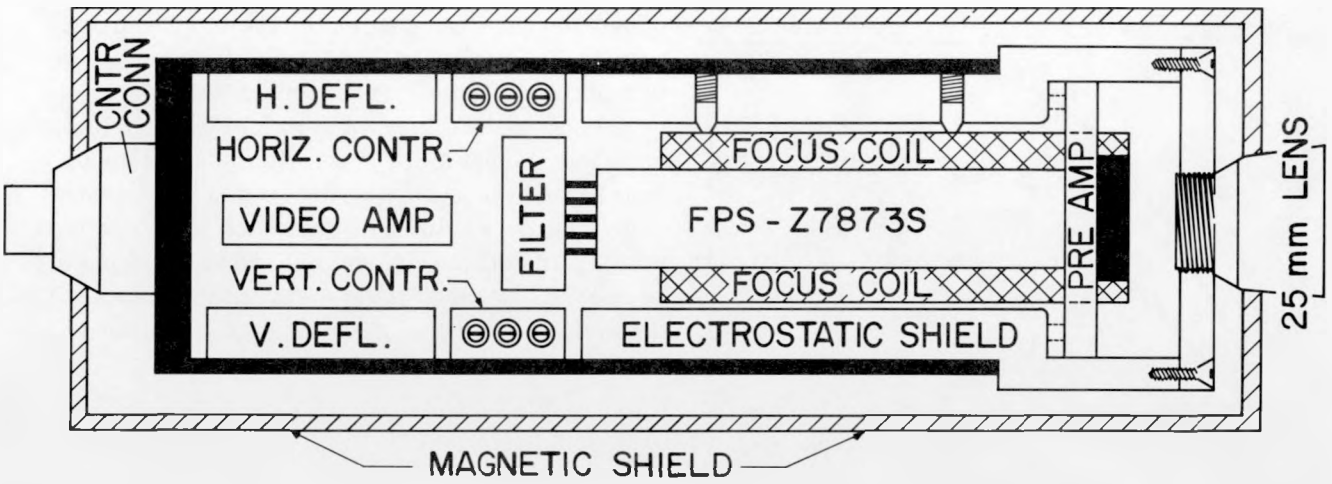

Fig. 7.
Component layout of the Model-1 FPS camera head.

as EDR cameras are usually located, the anticipated EMP would be of greater intensity than that encountered in the standard TV experiment box. EMP-induced disturbances have been observed in the EDR cameras as cable pickup of 2-3 V in amplitude and of >500 μs in duration. Because standard Pinex video signals are 3 V peak-to-peak into 50 Ω for maximum vidicon output, the cable pickup can be as large as the video.

To minimize EMP effects on the video envelope, the new camera output driver stage was designed to amplify normal composite video signals to 14 V peak-to-peak into 50 Ω. The amplified signals were attenuated after they were out of hostile environments and before they were recorded. Figures 10 and 11 show the actual EDR and FPS responses to EMP radiation during an underground experiment. The EDR camera of Fig. 10 was synchronized with the radiation, and a video gate in the amplifier chain (EMP gate) disabled the EDR video for about the first 400 μs after irradiation (period of maximum disturbance). The EDR camera was also located twice as far from the source as was the FPS camera. The FPS camera was not synchronized with the radiation

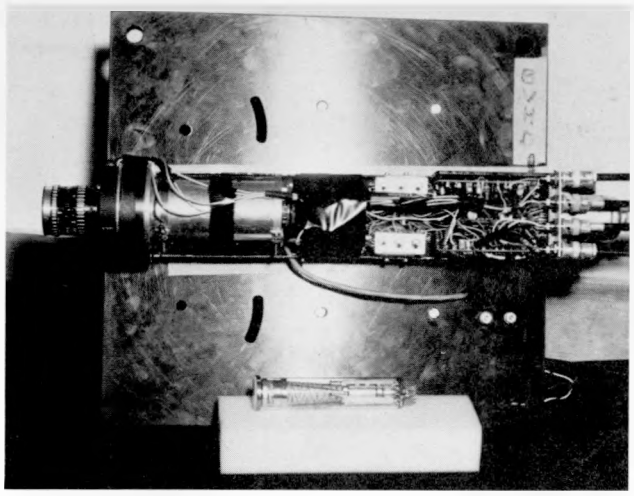

Fig. 8.
Model-1 FPS camera head assembly and Z7873S FPS vidicon.

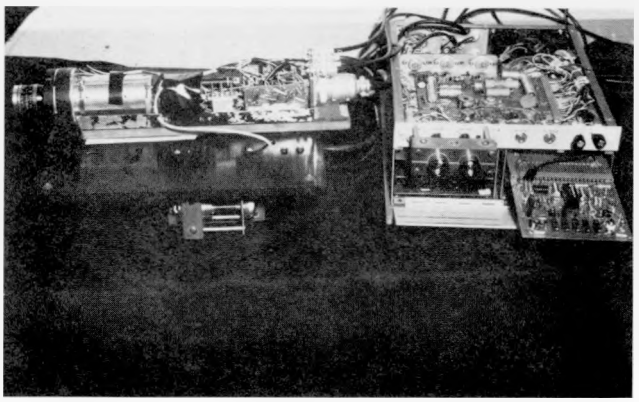

Fig. 9.
Model-1 FPS camera control unit (CCU) and head.

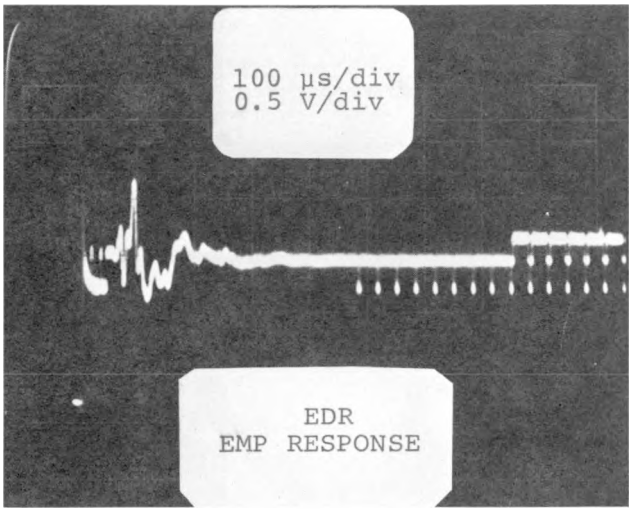

Fig. 10.
Observed EDR camera response to EMP-induced radiation during a standard Pinex experiment.

for this event (Fig. 11), nor was the FPS video disabled at any time during the period of maximum disturbance. The observed FPS perturbations confirm our predictions that the new output amplifier must be capable of more drive than that provided by the earlier EDR output amplifier. Some of the specifications of the completed camera are listed in Table II.

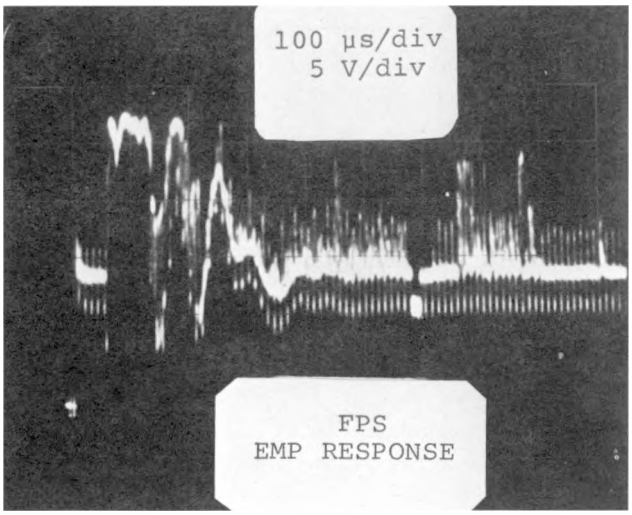

Fig. 11.
Observed Model-1 FPS camera response to EMP-induced radiation during close-in Pinex part of the same event described in Fig. 10.

The Model-1 FPS system block diagram is shown in Fig. 12. The electronic circuits were packaged in two chassis, the CCU and the head. The two chassis were connected with a multiconductor cable and several coaxial cables.

The sweep-generator block diagram is shown in Fig. 13. The linear voltage ramps were generated by integrating a constant current. The integration interval was determined by the vertical or horizontal drive frequency. The drive signals were used to discharge the integration capacitor through a field-effect transistor switch, thus terminating the integration period and initiating the next cycle.

The integration time constant (τ) was not continuously variable but rather could be selected in discrete combinations of R and C. This mode of selection was used to provide repeatability in the choice of τ for camera performance evaluations at various sweep rates.

The deflection-system electronics are shown in block-diagram form in Fig. 14. The push-pull output amplifiers were designed to amplify the input sweep voltage by a maximum factor of 10 (A_V = 2 to 10). The magnitude of the amplified voltage ramps was in the range of 25 to 125 V peak-to-peak. The vertical and horizontal amplifiers were identical. The amplifiers were designed to have a low output impedance because the FPS deflection inputs are basically capacitive loads.

During the short horizontal retrace intervals (0.5 µs), the amplifiers must drive the deflection inputs between the maximum and minimum ramp voltages ($\triangle V$ = 125 V, worst case). Therefore, the amplifier slew rate was designed to be at least 250 V/µs.

The horizontal and vertical position controls were referenced to about +300 V so that the deflection assembly resided at the proper voltage to conserve the internal FPS electrostatic fields that were required for the electron-beam optics. The ramps were then ac-coupled to the deflectron.

The cathode-blanking circuit is shown in Fig. 15. This circuit combines two blanking functions.

First, in order to prevent the FPS target from being damaged by a stationary (at least along one axis) read beam, a sweep-sampling circuit was designed to provide information on the sweep status. These signals, a +5-V bias if sweeps are active or a 0-V bias if sweeps are inoperative, were mixed with the normal dynamic blanking to provide static blanking if either sweep failed.

In the event of sweep failure, NOR gate G_1 (via A_2 and the first input of NAND gate G_2) drives Q_1 out of

TABLE II

SOME SPECIFICATIONS OF THE COMPLETED PROTOTYPE (MODEL-1) FPS VIDICON CAMERA

Vidicon	FPS, silicon-diode matrix target, 1-in.-diam, G.E. No. Z7873S	
Deflection	Electrostatic	
Focus	Electromagnetic	
Focus coil	Celco VFA2041	
Vertical period	2.8 ms total, 2.56 ms active, 256 lines	
Horizontal period	10 μs total, 9.5 μs active	
System video bandwidth	$\approx$5 MHz	
Video output	10 V peak-to-peak into 50 Ω plus 4 V sync	
Dynamic range	Between 64 and 128 (ratio of peak video to peak-to-peak noise)	
Sweeps	Remotely resettable	
Dimensions, HxWxL	(cm)	(in.)
Camera head	30 x 6.3 x 6.3	12 x 2.5 x 2.5
CCU	12.5 x 27.5 x 35	5 x 11 x 14

saturation, thus biasing the FPS cathode to +47 V and disabling the read beam.

Second, the normal composite blanking signal is used to bias the FPS read beam to cutoff during the camera's retrace intervals. This is accomplished by driving Q_1 (via A_1 and the second input of G_2) with the composite blanking signal. This, of course, requires that the first input of G_2 be enabled. If both sweeps are operational this input is biased positive, permitting the blanking pulses to get through the gate.

III. CALIBRATIONS

A transfer curve (output video signal vs input radiant flux) was generated. The transfer curve (Fig. 16) is given with the spatial frequency in the scene imaged on the FPS target as a parameter. The abscissa f-numbers correspond to lens-aperture settings for the measurement.

Spatial frequency determination is best discussed in the more general context of horizontal resolution. Adjacent black-and-white bars of various widths were used as a test pattern to determine the horizontal resolution. Figure 17 is a diagram of the experimental setup. The test pattern is formed by strips of black printed-circuit-card layout tape on a piece of clear plastic 1.6-mm (1/16-in.) thick. The oscilloscope displays one line of video through the center of the test target. Relative video-signal amplitudes resulting from the various bar spacings are read directly off the oscilloscope. The resulting contrast-transfer-function (CTF) curve and the calculated modulation-transfer-function (MTF) curve are shown in Fig. 18. Some important observations are as follows.

1. The 1.6-mm (1/16-in.) bars in a 152-mm- (6-in.) wide field of view (FOV) were resolved with approximately 30% amplitude modulation. The 1.6-mm bars correspond to 0.32 1p/mm (8 1p/in.) resolution at the radiation-to-light converter, for a total of

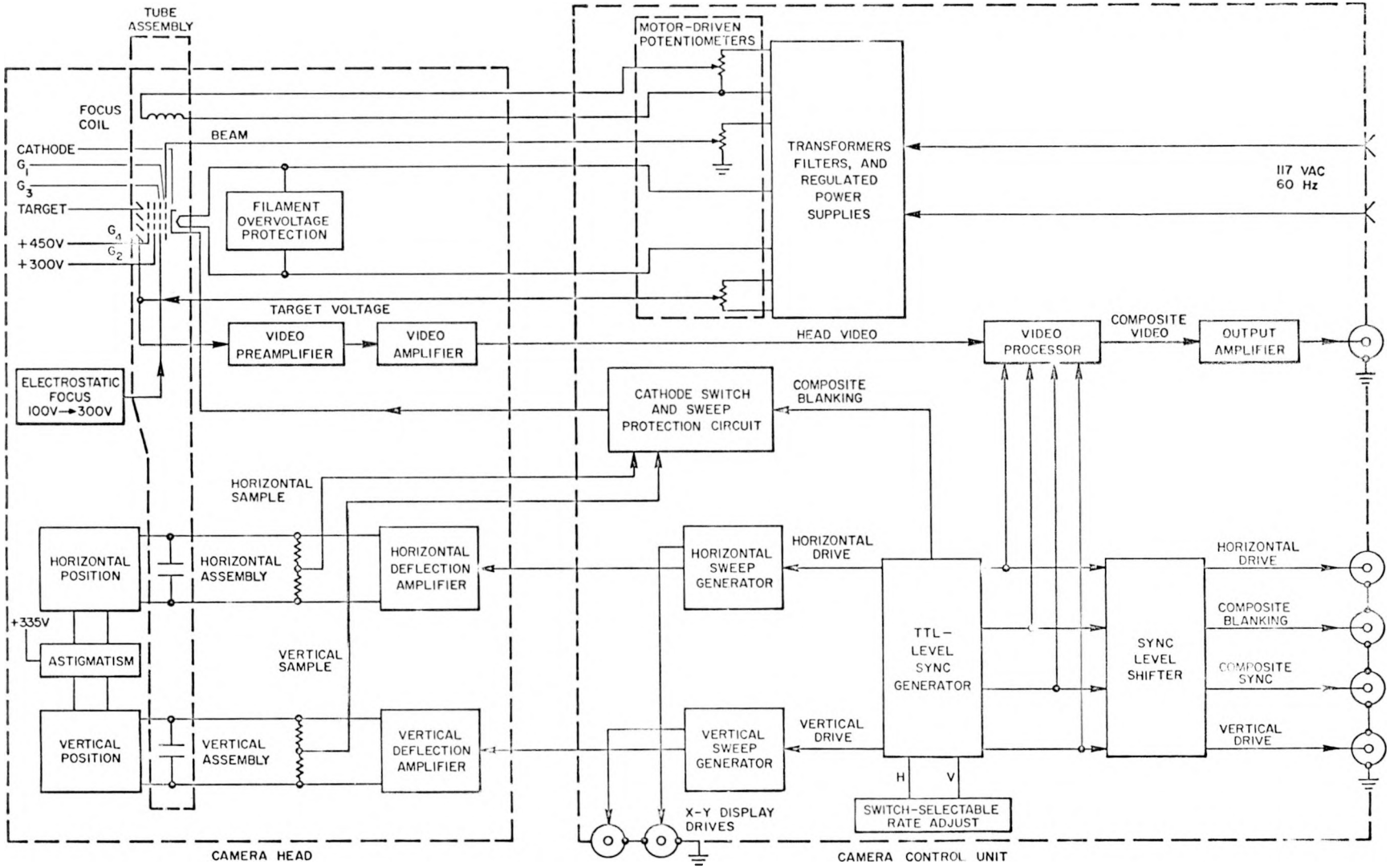

Fig. 12.
Simplified block diagram of Model-1 FPS camera.

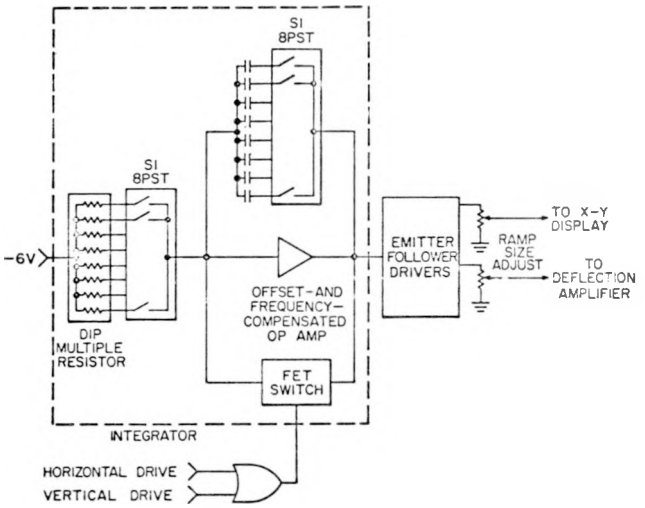

Fig. 13.
Variable-rate analog sweep generator. Horizontal and vertical generators are identical except for component values. S1 and S2 are dip-compatible 8PST passive switches.

32 line pairs (1p) across the 102-mm- (4-in.) diam converter.

2. The 0.8-mm (1/32-in.) bars, corresponding to 64 lp/mm (16 lp/in.), were not resolved. The estimated limiting (5% modulation) resolution was 0.48 lp/mm (12 lp/in.), so that the estimated limiting horizontal resolution across the converter was 48 lp.

3. The camera optical system magnification was approximately 1/25. This scales the 0.32 lp/mm (8 lp/in.) and the 152-mm (6-in.) FOV at the converter to 8 lp/mm (203 lp/in.) and 6.1 mm (0.24 in.) respectively, at the vidicon target.

The relative spatial frequency, f_s, at the vidicon target can be calculated by

$$f_s = \frac{\text{resolution x FOV width}}{\text{horizontal line length}} ,$$

from which f_s = 49 lp/line. The total horizontal line duration is 10 μs, of which the active sweep time, t_s, is 9.5 μs. Thus the limiting video frequency is $f_v = f_s/t_s \approx 5.2$ MHz. This limiting video frequency is not the upper −3 db frequency, but rather is the frequency at which unity signal-to-noise ratio occurs. The result is consistent with the experimental data, because the highest observed frequency (the 1.6-mm bars) in the video, at about 30% modulation, was almost 5 MHz. The observed bandwidth is assumed to be limited by the video amplifiers, which were retained from the EDR camera.

Because the downhole experiment used beam-splitting optics, two images of the converter were formed on the FPS target. The experimental arrangement is diagrammed in Fig. 19. The setup represents a typical optical-system configuration for an event. The light pattern from the test fixture falls on the incident mirror, located at 45° to the test-fixture longitudinal axis. The two beam-splitting mirrors are located so that the camera can view an image on each, and so that the junction of the two beam-splitting mirrors is at the vertical centerline of the camera's field of view. These two mirrors are positioned slightly over and slightly under 45° from the camera's longitudinal axis. The optical path length from the test fixture to the camera lens is about 61 cm. An ND filter placed over half of the vidicon target increases the tube's dynamic range by making one image dimmer than the other. For the event, the test fixture is removed and is replaced by the NE-102 radiation-to-light converter.

There were approximately 120 scan lines per image. The vertical resolution is given by[13]

$$\text{vert. resolution} = \frac{0.7 \text{ x number of lines/image}}{\text{number of lines/line pair}} ,$$

or 42 lp/image (two lines per line pair) with the present system.

We generated a transfer curve for the event (output video signal vs input radiant flux calibrated in per cent of expected light intensity) (Fig. 20). The curve was obtained using a calibrated General Radio Type 1539-A Stroboslave as the light source, with appropriate ND filters, diffusers, beam-splitting mirrors, and the blue transmission filter between the light source and the FPS camera. The light-source intensity and spectral characteristics were calibrated, as above, to approximate the expected light pulse from the NE-102 converter. The imaged optical scene from one of the mirrors was attenuated by placing an ND filter over that area of the FPS target. The camera lens aperture (f-stops) was then varied so that the camera was subjected to incident light in the range 3.12-400% of that expected. Figure 21 shows portions of two different video scan lines obtained during the calibration.

Figures 22 and 23 show TV fields with different input light levels. The two fields of Fig. 22 represent the first TV frame after the calibration light source

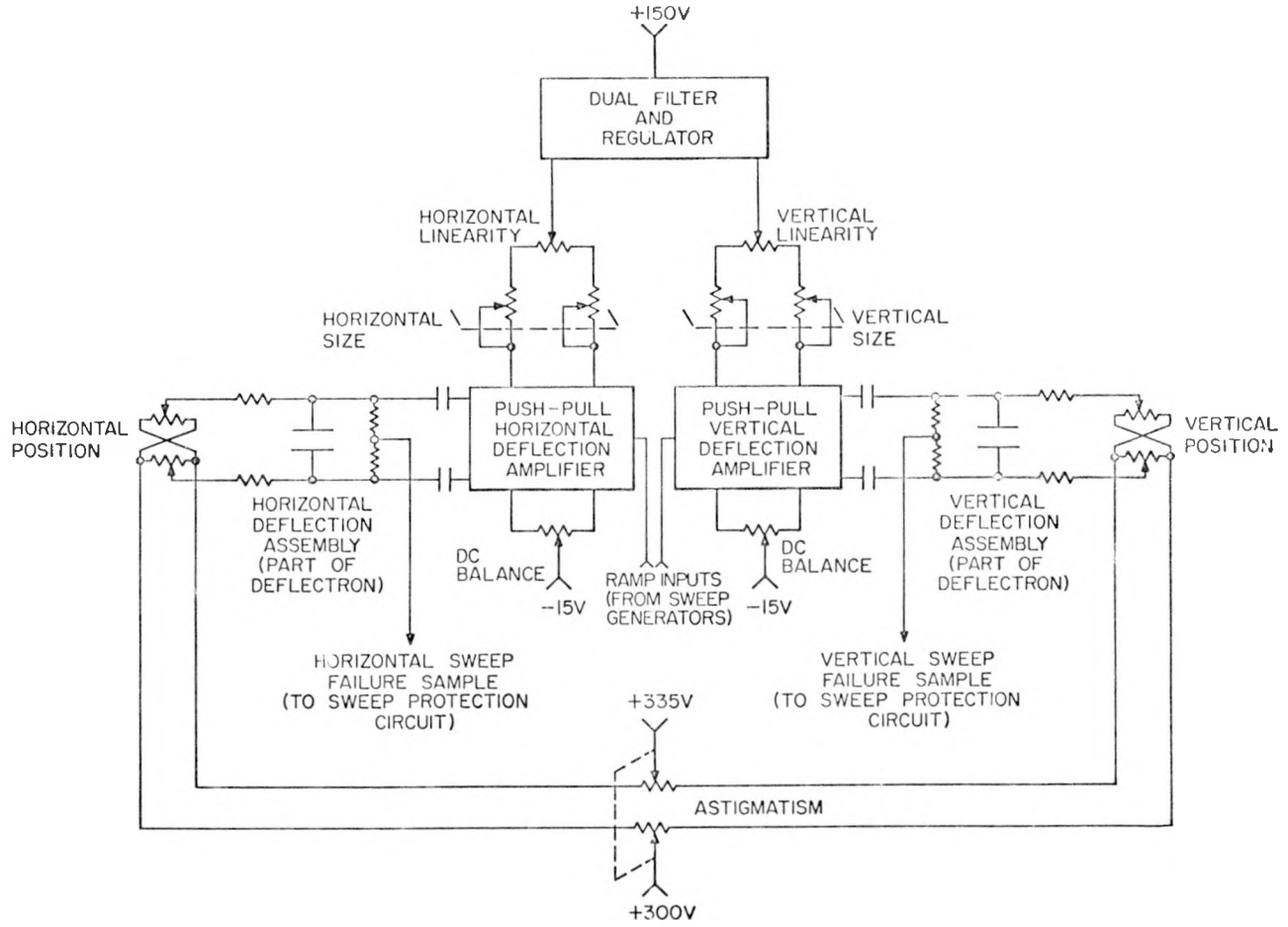

Fig. 14.
Model-1 FPS deflection scheme.

was strobed. The light source, again the Stroboslave, was pulsed during the vertical sync interval just preceding the first field shown. Each field contains optical information from the two different mirrors that comprise the beam-splitting optics used in the

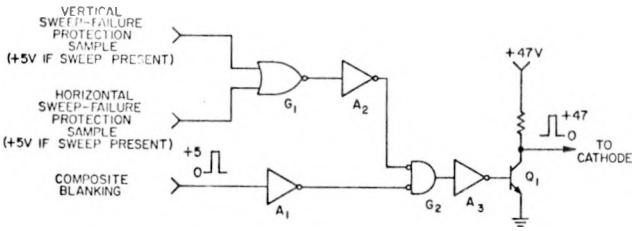

Fig. 15.
Cathode-blanking circuit, shown with waveforms present during dynamic blanking and with implied static inputs from the sweep-failure circuitry.

experiment. One image was covered with an ND filter. The smaller amplitude signals in the early part of the field are from the filtered image, and the two larger signals are from the unfiltered image. The unfiltered image is just below the saturation level. The camera lens aperture was set at f/4. The pertinent data for Fig. 23 are the same as for Fig. 22, with the exception that the camera lens aperture was set at f/2.8. Now the filtered video signals are of larger amplitude. The unfiltered video signals, however, are of smaller amplitude, and the peaks are inverted. The saturation effect in the unfiltered image is shown in these photographs and also on the event transfer curve. This effect has been discussed elsewhere[15] and is mentioned briefly in Appendix B.

The overall system dynamic range (with beam-splitting mirrors) is the composite range of the two curves and is between 128 and 256. The lens aperture

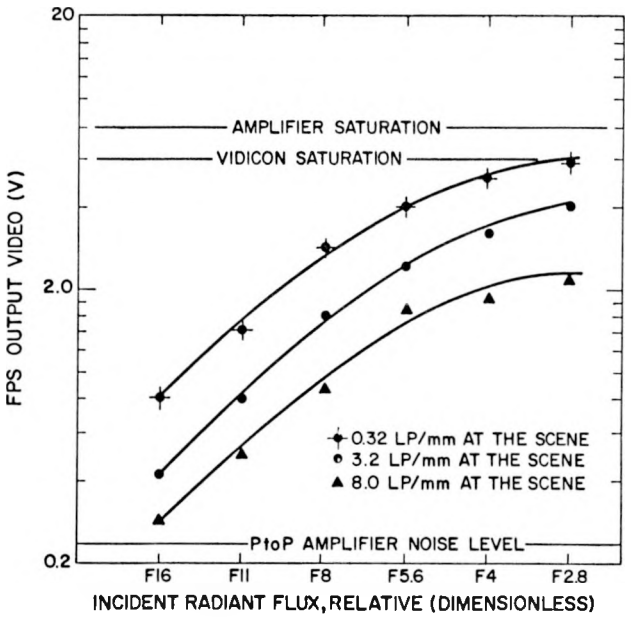

Fig. 16.
FPS camera output video signal as a function of input radiant flux and as a function of spatial frequency in the scene.

was set so that the camera's dynamic range centered on the 100% point of Fig. 20 for the event.

IV. CONCLUSIONS

The prototype ultrafast-scan camera using an FPS vidicon tube showed good promise in its successful field test.[16] The camera operated in its close-in position with adequate resolution and dynamic range, acquiring data comparable to that obtained from an EDR camera located much farther from the device. The good results were obtained in spite of the 2.8-ms data field readout time, the presumably more severe EMP environment, and the relatively crude camera circuit designs, including the inadequate-bandwidth amplifiers. Actual camera performance was, of course, inferior to the theoretical maximum and to some design expectations. Insufficient time prior to the downhole experiment and inexperience in certain areas of TV camera design prevented full utilization of the FPS vidicon potential. A Model-2 camera is presently being designed as a totally new unit. It will offer performance that is improved significantly over that of the prototype.

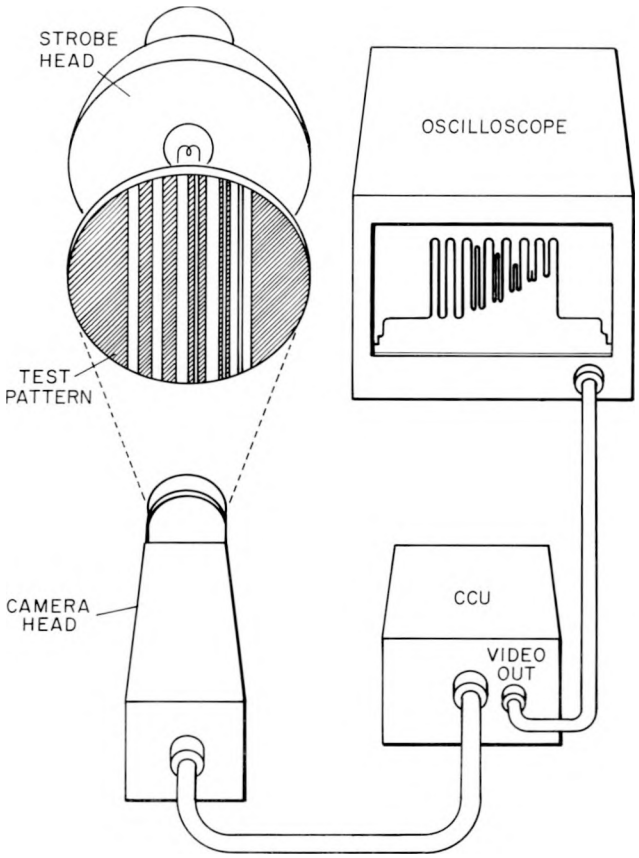

Fig. 17.
Artist's conception of test-pattern setup for obtaining the FPS camera CTF (not to scale).

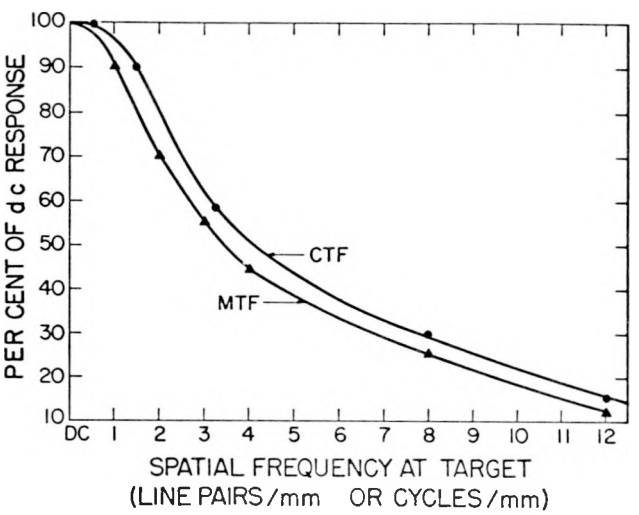

Fig. 18.
CTF and MTF curves for Model-1 FPS camera.

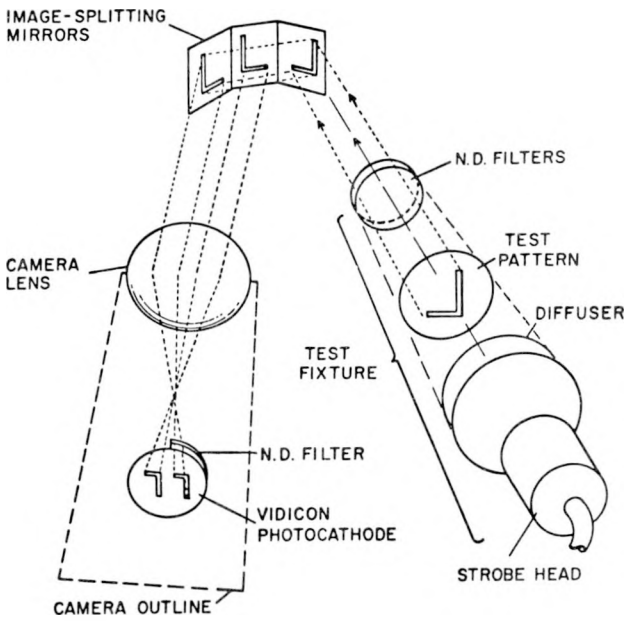

Fig. 19.
Artist's conception of simplified version of calibration setup on the close-in TV package (not to scale). Reversed Ls used only to show optical paths of light rays in the split-mirror system. A suitable test pattern was used in the actual calibration. Direction of view is approximately from the source location.

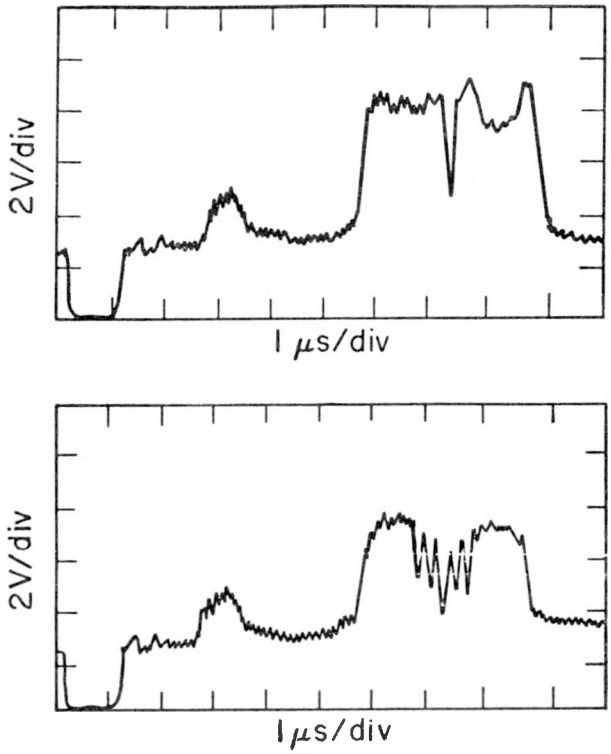

Fig. 21.
FPS video signals of two different horizontal scan lines that represent two different spatial frequencies in the scene.

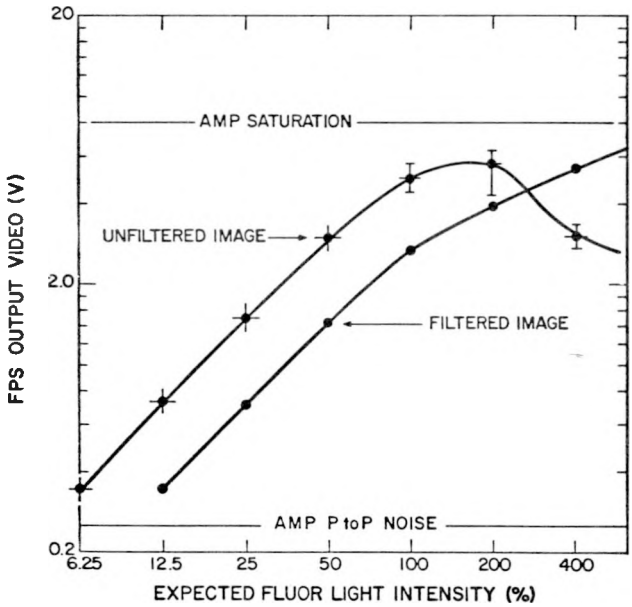

Fig. 20.
The event transfer curve.

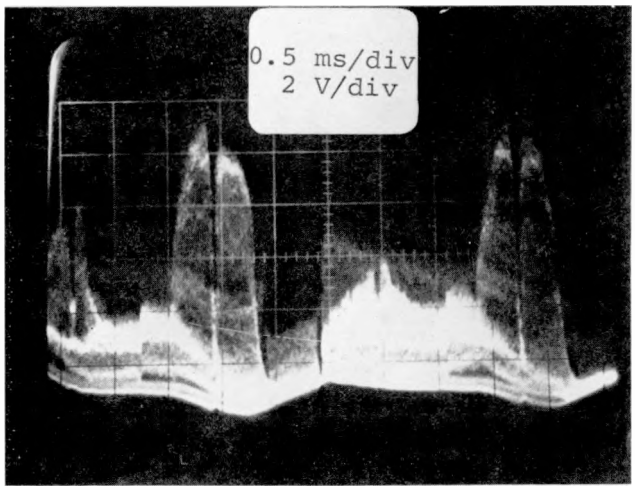

Fig. 22.
Two consecutive FPS TV fields. Lens aperture at f/4.

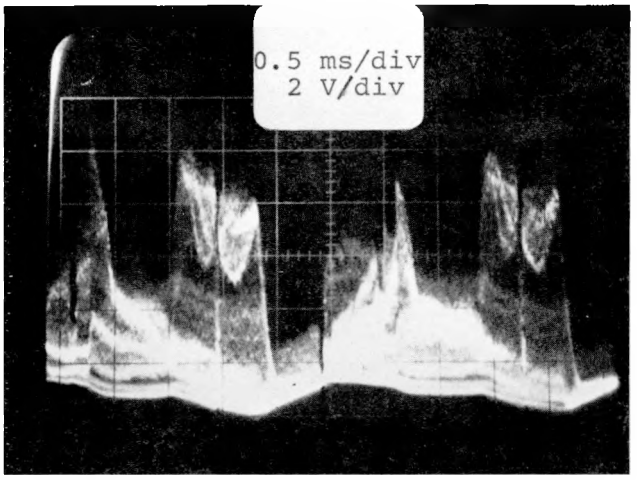

Fig. 23.
Two consecutive FPS TV fields. Lens aperture at f/2.8.

ACKNOWLEDGMENTS

The authors wish to acknowledge engineering and technical support by J. Garcia, J. H. Calligan III, and G. Barber, LASL; and E. Wilson, G. Simon, and A. Kvanvig, EG&G /NTS. We also wish to acknowledge helpful discussions and advice from M. Cates, as well as thank him for the opportunity to use the FPS camera as part of his downhole experiment.

APPENDIX A

LIMITATIONS OF ELECTROMAGNETIC-DEFLECTION SYSTEMS

In conventional magnetic-deflection systems, the beam deflection is produced by a sawtooth magnetic field from a deflection coil. The deflecting field is generated by a current ramp that varies approximately linearly with time.

The deflection current required is a function of the vidicon tube dimensions, the deflection angles required to produce a given raster format and size, the tube electrode voltages, the electron optics configuration of the particular tube, and the deflection coil characteristics. Calculation of the maximum energy stored in an ideal deflection coil[17] takes these factors into account in the equation

$$W_p = \frac{1.4 \times 10^{-5} a^2 \sin^2 \alpha_m V_c}{\ell_o} = 1/2\ LI_p^2 \quad ,$$

in mks units, where

V_c = vidicon anode voltage,

a = inner radius of deflection coil,

ℓ_o = effective length of deflection coil, including the effects of the fringing magnetic field,

α_m = maximum deflection angle (measured from the tube longitudinal axis),

L = deflection coil inductance,

and

I_p = current required for maximum deflection angle.

The peak current in the horizontal deflection coil is

$$I_p = \frac{1}{L} \int_{t_o}^{(t_s/2)} V_{defl}\, dt + I_o \quad .$$

In this definition,

t_s = the active horizontal sweep interval,

t_o = the time during t_s when the deflection current is zero,

I_o = 0, the current at t_o, and

V_{defl} = the constant deflection voltage.

Since the peak current occurs at $t_s/2$, the expression reduces to

$$I_p = \frac{V_{defl}}{L} \frac{t_s}{2} \quad . \tag{A-2}$$

The deflection voltage is proportional to the coil inductance multiplied by the time rate of change of current in the coil. The deflection voltage and peak current, determined once the coil inductance and scan rate have been chosen, determine in turn the energy stored in the coil. Clearly, the horizontal scan parameters place more stringent demands on the electronics than do the much slower vertical rates. In the design of a practical deflection system, the flyback (retrace) time, t_r, and the active horizontal sweep interval, t_s, are both fixed by the application.

Two major problems arise when the scan rate is increased if the same raster size is desired (α_m remains constant). One concerns generating the same magnitude current ramp in a shorter time. According to Eq. (A-2), if the horizontal sweep time is reduced by about a factor of three (from 29.3 μs for the EDR camera to 9.5 μs for the FPS camera) then either the deflection voltage must be increased or the inductance must be decreased by that factor. But according to Eq. (A-1), for a given deflection the inductance cannot be decreased without increasing I_p, an increase that is undesirable because of consequent increased power dissipation in the coil as well as in the driving-circuit transistors. Moreover, when modifying an existing camera system is the design goal, the coil inductance is fixed by the existing coil configuration. Therefore the driving voltage, V_{defl}, is the only parameter that can be increased. This also causes transistor power dissipation, but not coil dissipation, to increase.

A second problem encountered when t_s is reduced is that t_r must (or should) also be reduced proportionately, so that the ratio of active sweep time to retrace time remains constant. Otherwise, too much of the total sweep time is taken by retrace, resulting in inefficient use of the small total sweep time that is available. The total field time T_F, exclusive of vertical flyback and vertical interval, is $N(t_s + t_r)$, where N is the number of lines. The horizontal flyback time is some constant fraction, p, of t_s. Thus

$$T_F = N(t_s + pt_s) = Nt_s\,(1 + p) \quad . \tag{A-3}$$

The portion of T_F which can contain useful information is Nt_s. Solving Eq. (A-3) for Nt_s, we have

$$Nt_s = \frac{T_F}{1 + p} \approx (1 - p)T_F \quad ,$$

where the approximation holds for small p. It is clear that if p is held constant for shorter field time, the total information content decreases linearly with T_F for a given bandwidth. This linear decrease is the cheapest price paid for reducing the field time. Now consider instead a constant t_r. Then

$$Nt_s = T_F - Nt_r \quad .$$

In this case the information content decreases not only with T_F but also with the number of lines, which is self-defeating.

The flyback voltage pulse, V_{fb}, that is generated during retrace time is

$$V_{fb} = V_{defl} + I_p \pi L \frac{1}{t_r} \quad , \tag{A-4}$$

which is linear in reciprocal t_r. It is evident that if t_r changes to $t_r/3$ (from 3 μs for the EDR to 1 μs for the FPS camera*), if $t_s \gg t_r$, and if I_p and L are held constant, then V_{fb} increases by nearly a factor of three. This pulse is impressed across the deflection transistor. The transistor must be capable of withstanding this increased voltage. A typical flyback voltage pulse (for an EDR camera with t_s = 3 μs) is shown in Fig. A-1 as V_{max}. The figure also shows the current waveform. A simplified output stage of a transistor deflection amplifier and its deflection coil appear in the inset of the figure. V_{min} is the voltage across the drive transistor during the active portion of the sweep cycle. V_{max} is the flyback voltage which is generated in the retrace portion of the sweep cycle: $V_{fb} = L(|I_p| + |-I_p|)/t_r$. During t_r the deflection current undergoes a maximum change in a minimum time, decreasing rapidly from $+I_p$ to $-I_p$. These currents, typically centered on zero, are the peak values of the deflection current.

Another consequence of the faster scan rates is that the parameters must be adjusted in the face of increased high-frequency-content requirements.

**As finally designed, the FPS camera actually had a 0.5-μs horizontal flyback time.*

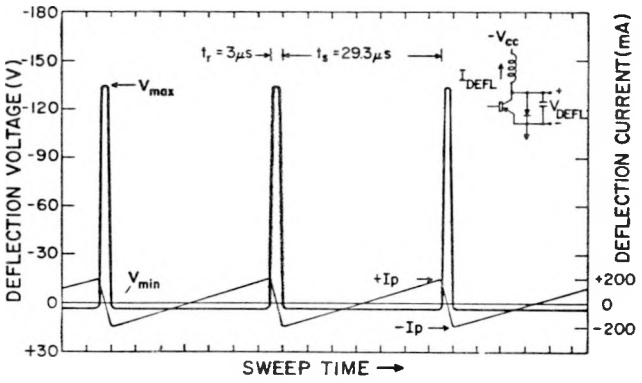

Fig. A-1.
Typical idealized voltage and current waveforms in electromagnetic-deflection systems. Indicated values are for EDR-camera overscanned format discussed in connection with Table A-1.

This fact is made clear by considering the Fourier-series representation of the sawtooth deflection waveform. The number of harmonics needed to approximate the waveform is unchanged as long as the ratio t_s/t_r remains constant, but the harmonics are all of higher frequency for the faster sweep times. Thus higher frequency response is required from the amplifiers, while at the same time the voltages and power levels are increased.

The EDR vidicon camera was investigated for possible use at the proposed higher scan rates. Two scan formats, both of potential value in our program, were evaluated: (1) the industry standard of 9.6 mm (3/8 in.) in the horizontal direction and 12.5 mm (1/2 in.) in the vertical direction for an aspect ratio of 3 to 4; and (2) the overscanned format where a square raster 25 mm (1 in.) by 25 mm (1 in.) is used to assure that the raster overlays the entire photosensitive area of the target. Table A-I compares experimentally observed flyback voltages with those calculated from Eq. (A-4).

If t_r is reduced in order to maintain the same ratio of t_r to t_s as before (say, from 3 μs to 1 μs), Eq. (A-4) shows that V_{fb} will increase in absolute value from 58.3 V to 175 V for the 3 by 4 format and from 129 V to 387 V for the overscanned format.

The problems outlined above make magnetic-deflection systems particularly unattractive at the higher scan rates. Indeed, these problems may be severe enough that their solution is impractical at the present component state-of-the-art, even with totally new magnetic-deflection circuit designs. Their solution in terms of modifications of an existing design is out of the question. The other alternatives (electrostatic deflection and focus, and FPS) were examined for this reason.

TABLE A-I

OBSERVED ELECTROMAGNETIC DEFLECTION CURRENTS AND VOLTAGES AS FUNCTIONS OF RASTER FORMAT, RASTER SIZE, AND RETRACE INTERVALS

Parameters	Horizontal 9.6 mm (3/8 in.)	Vertical 12.8 mm (1/2 in.)	Horizontal 25.4 mm (1 in.)	Vertical 25.4 mm (1 in.)
Deflection Voltage	+6.0 V	+6.0 V	+12.0 V	+16.0 V
Peak Deflection Current	$\pm 100 \times 10^{-3}$ A	$\pm 36 \times 10^{-3}$ A	$\pm 200 \times 10^{-3}$ A	$\pm 96 \times 10^{-3}$ A
Predicted V_{fb}	-58.3 V	-20.7 V	-128.6 V	-55.2 V
Observed V_{fb}	-62 V	-20 V	-130 V	-54V

APPENDIX B

SOAK TIME

If a nonsaturating unit-step function of light floods a vidicon target, the output signal caused by the scanning beam is observed to rise with time, t, roughly as $(1-e^{-t/\tau})$, where the response time τ is commonly known as the "soak" time. Soak time is not often mentioned in the literature because it is relatively unimportant in many continuous-field* applications when compared with the total image lag (which occurs with scan-off after light is *removed*). However, in single-field experiments, if the beam scans over a part of the field that contains written data before the transient data has finished soaking, the data will be in error. Soak times as short as possible are therefore desirable. We will review the processes involved in determining the soak time in a simplified qualitative way in order to show why the soak time is usually shorter with silicon-diode matrix targets than it is with Sb_2S_3 targets. Details elaborating on most of the following discussion can be found in the literature.[18-21]

Put briefly, the reason for the different soak times in the two types of targets lies in the fact that Sb_2S_3 targets operate by photoconduction while silicon targets operate as p-n junction devices.

Photoconductive processes have been studied in detail.[22-26] Many different processes and their characteristics have been identified. Some of the characteristics of the Sb_2S_3 photoconductive materials used as targets in vidicons can be appreciated easily by recalling how the targets operate.

Consider the simplified diagram, Fig. B-1,[27] of the target region of a Sb_2S_3 target vidicon. Assume the tube has been operated in the dark long enough that the carrier concentrations have reached thermal equilibrium. The scanning beam has deposited a sufficient number of electrons on the scanned surface of the photoconductor to charge it to the cathode potential ($\approx$0 V). Because of the potential difference between this surface and the front surface, there is a large electric field across the slab. Assume for simplicity that one carrier type, say holes, dominates. In the dark, the target is an insulator, with the number of free holes/cm^3, p, of the order 10^5. The current flow in this condition is due only to the

As opposed to single-field, as in TV Pinex experiments.

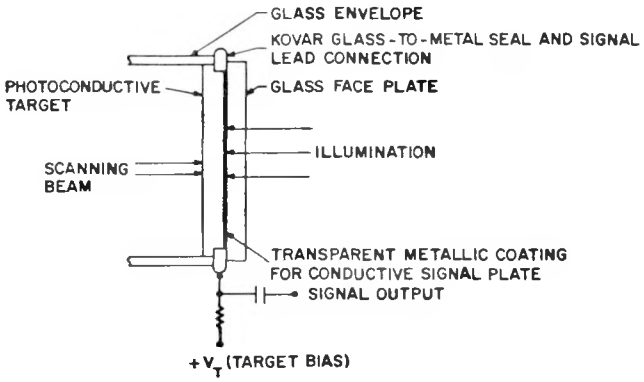

Fig. B-1.
Simplified schematic cross-section of a photoconductive-target vidicon target (after Ref. 27).

carriers that can be injected by either contact.* In insulators with "good" (e.g., ohmic) contacts, this current density is space-charge-limited and is therefore given by[28]

$$J_d = (8/9)\ (\epsilon\mu/L^3)V_T^2 \quad ,$$

where

ϵ = material permittivity,
μ = carrier mobility,
L = target thickness,

and

V_T = target voltage.

The dark current is thus sublinear with voltage ($J_d \propto V_T^2$).

Now consider applying to the target a step function of light of the proper wavelength. By "proper" wavelength we mean one that excites hole-electron pairs with good quantum efficiency. If the optical absorption coefficient of the target is very high, the carriers will all be generated near the surface, and the photocurrent will also be space-charge-limited to

The beam obviously acts through a contact, albeit not a metallurgical one.

negligible values so that low sensitivity results. Getting the highest sensitivity thus requires that the absorption coefficient be small enough that the target is essentially volume-excited (that is, uniformly illuminated through the entire thickness) but large enough that nearly all of the light is absorbed in the target so that the quantum efficiency approaches unity.

Figure B-2 contains idealized diagrams of the energy band structure in a photoconductor with an applied field. The diagrams assume perfect contacts, which never exist in practice.[23] In the trap-free material, diagram (A), the only energy levels in the forbidden gap belong to recombination centers of energy E_R. Since the material is volume-excited, carrier transport is only by drift in the electric field. Carriers that are generated drift as shown. Positive charge accumulates on the scanned surface (and the bands bend accordingly, though this is not shown) until electrons are injected by the beam, at which time recombination can occur through the levels at E_R. The response time therefore depends only on the average time required for holes to reach the beam-side contact. This time depends on the hole velocity, which is, in turn, dependent on the hole mobility for a given applied electric field. In the trap-free material, the mobility is high. But it is characteristic of vidicon targets that the trap concentration is high (greater than about $10^{16}/cm^3$), possibly owing to the microcrystalline nature of the as-grown material. In the single-level trap model, diagram (B), there are deep traps at the level E_T in addition to the recombination centers. Holes that are generated by the illumination have a very high probability of being trapped after traveling only a short distance. Once trapped, the carriers are not easily thermalized because the traps are deep, and once the carriers are released, they are easily trapped again. Consequently, their mobility is several orders of magnitude lower than in trap-free material. This leads to a long response time, and the response time clearly determines the soak time.

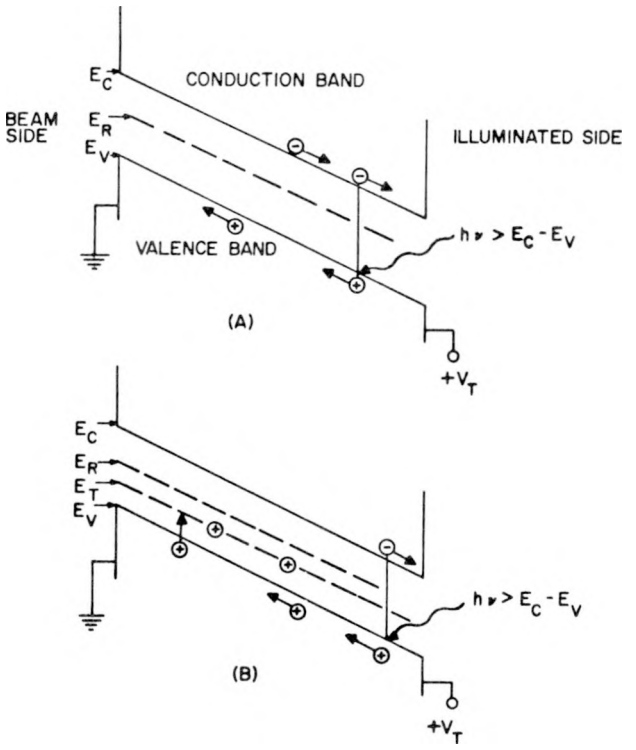

Fig. B-2.
Idealized diagrams of energy band structure in photoconductor for (a) trap-free and (b) single-level-trap cases. Both trap-free and single-level trap models simplified compared with realistic models.

The silicon-diode matrix vidicon target is shown in schematic cross section in Fig. B-3. In this simple version, diodes are formed in the n-type substrate by diffusing p-type dopants through the thermally grown SiO_2 by using photoresist techniques, thereby forming junctions by a standard planar process. The SiO_2 layer surrounding the diodes shields the n-type material from the scanning beam. In the dark, the scanning beam sets all the p-type surfaces to ≈ 0

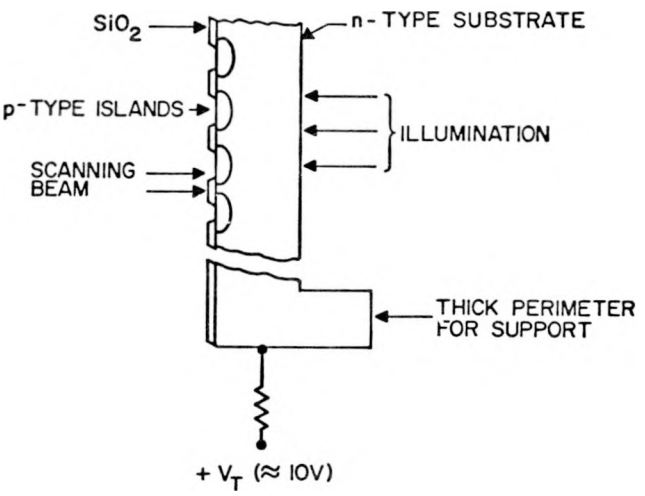

Fig. B-3.
Schematic cross-section of early version of silicon-diode matrix vidicon target (after Ref. 29).

volts and the diodes are consequently reverse-biased. The dark current density in this case is approximately the sum of the contribution, J_{sat} (the reverse-bias leakage current) from each diode owing to thermally generated carriers. The dark current can therefore be very low, on the order of a few nanoamperes, in contrast to the relatively high dark current in photoconductive targets.

An approximate hole concentration sketch is shown in Fig. B-4. The point x = 0 is at the illuminated surface of the target. The total hole density, p_n, is plotted qualitatively vs distance into the material using time as a parameter. Curves A and B are plotted at times $t = t_0^-$ and $t = t_0^+$, respectively, just before and just after the unit-step function of light is applied. At $t = t_0^-$, hole density is the thermal equilibrium value, p_{no}, everywhere in the bulk material except near the reverse-biased junction depletion region. Because there is no electric field in the n-type bulk material, space-charge-limiting does not occur. Assume that the surface recombination has been minimized, and that the hole diffusion length, L_p, is long relative to the material thickness. Then even though the holes are generated only near the surface in silicon, nearly all will reach the junction. Typical target thicknesses in the diode region are 5-50 μm[29] and typical room-temperature hole diffusion lengths in n-type silicon are in the range 10-1000 μm, so it is easy to design targets such that L is the required factor of three or so less than L_p.

That most of the light is absorbed near the surface is evident by considering that the absorption coefficient for silicon at 1.9 eV (near the peak response) is about 3×10^3 cm^{-1}.[30]

Curve B in Fig. B-4 shows the situation at $t = t_0^+$, just after the unit-step function of light is applied. Here $\Delta p(0)$ is the excess hole density generated by the light. Very few holes diffuse toward the junction (because of the nonequilibrium conditions) instantaneously because of the nonzero time required for the hole concentration to return to thermal equilibrium. Those that do reach the junction are swept across the approximately 5-μm-wide depletion region in very short transit times (several picoseconds). The transit time across the junction therefore contributes negligibly to the soak time, and the major contribution to the transit time is caused by carrier diffusion and dielectric relaxation.

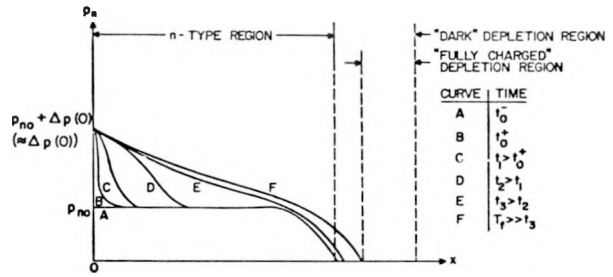

Fig. B-4.
Qualitative diagram of hole concentration vs distance in silicon-diode matrix target with time as a parameter.

As soon as the carrier concentration has been disturbed sufficiently throughout the bulk region (curves C and D), the soak period is essentially over. This occurs quickly, probably of the same order as the minority-carrier lifetime (a few microseconds), but perhaps approaching the dielectric relaxation time (of the order of 1 ns). It follows that the soak time in silicon-diode-matrix vidicons is negligible in many applications, at least when compared with the soak time in Sb_2S_3-target tubes.

Full charge storage occurs (curves E and F) after the soak time is over and the junction width starts to decrease as the p-type bulk region becomes positively charged.

If the light is sufficiently intense, the p-side of the diodes can become so positively charged in a frame that the electric field owing to the positive charge turns back the beam. In effect, this makes the normally electron-injecting contact at the surface become a blocking contact. In this saturated state, the beam cannot neutralize the charge, and the signal current has the opposite polarity from that occurring below saturation. Experimental observation of this effect appears in the bottom right-hand reproduction in Fig. 4, where the effect of the bar shows a polarity reversal.

REFERENCES

1. G. J. Yates, "Fast-Scan TV System," LASL internal document, unpublished, 1972.

2. M. R. Cates and B. W. Noel, LASL internal memorandum, unpublished, 1974.

3. K. Schlesinger and R. A. Wagner, "A Mixed Field Type of Vidicon," IEEE Trans. Electron Devices *ED-14*, 163-170 (1967); also, K. Schlesinger and R. A. Wagner, "A Mixed-Field Device for

Simultaneous Focus and Deflection," in A. B. El-Kareh, Ed., Proc. Electron and Laser Beam Symp., PA State Univ., March 31-April 12, 1965, pp. 471-488.

4. I. T. Saldi and K. Schlesinger, "The FPS Vidicon," Optical Spectra **4**, 53-56 (February 1970).

5. D. B. Hunter, "Supertube," Optical Spectra **9**, 39-41 (November 1975).

6. D. B. Hunter, private communication, April 1976.

7. RCA Electronic Components, data sheet for 8507A Sb_2S_3 vidicon.

8. GE Imaging Devices, data sheet for 8573A Sb_2S_3 vidicon.

9. GE Imaging Devices, data sheet for Z7873S silicon-diode matrix FPS vidicon.

10. GE Imaging Devices, data sheet for Z7801 Sb_2S_3 FPS vidicon.

11. RCA Electronic Components, data sheet for 8573A Sb_2S_3 vidicon.

12. RCA Electronic Components, data sheet for 4532A silicon-diode matrix vidicon.

13. Nuclear Enterprises, Inc., Plastic Scintillators catalog.

14. R. E. Johnson, "Silicon Diode Array Target Vidicons," RCA Application Note AN-4623.

15. E. C. Douglas, "High Light-Level Blooming in the Silicon Vidicon," IEEE Trans. Electron Devices *ED-22*, 224-234 (1975).

16. M. R. Cates, G. J. Yates, and B. W. Noel, unpublished data, 1975.

17. R. Dressel, "Deflection Coils," in T. Stoller, M. A. Starr, and G. E. Valley, Jr., Eds., *Cathode Ray Tube Displays* (McGraw-Hill Book Co., Inc., New York, 1948), pp. 303-308.

18. L. Heijne, "Photoconductive Properties of Lead-Oxide Layers," Philips Res. Repts., Suppl. 4, 1-161 (1961).

19. S. V. Forgue, R. R. Goodrich, and A. D. Cope, "Properties of some Photoconductors, Principally Antimony Trisulfide," RCA Rev. **12**, 335-349 (1951).

20. L. Heijne, "Physical Principles of Photoconductivity I: Basic Concepts; Contacts on Semiconductors," Philips Tech. Rev. **25**, 120-131 (1963/1964); "II: Kinetics of the Recombination Process; Sensitivity and Speed of Response," Philips Tech. Rev. **27**, 47-61 (1966); "III: Inhomogeneity Effects," Philips Tech. Rev. **29**, 221-234 (1968).

21. R. W. Redington, "The Transient Response of Photoconductive Camera Tubes Employing Low-Velocity Scanning," IRE Trans. Electron Devices *Ed-4*, 220-225 (1957).

22. H. Miller and J. W. Strange, "The Electrical Reproduction of Images by the Photoconductive Effect," Proc. Phys. Soc. (London) **50**, 374-384 (1938).

23. A. Rose, "An Outline of Some Photoconductive Processes," RCA Rev. **12**, 362-414 (1951).

24. H. Keiss and B. Binggell, "Speed of Response of Photocurrents in CdSe," RCA Rev. **36**, 485-498 (1975).

25. A. Rose, "Maximum Performance of Photoconductors," Helv. Phys. Acta **30**, 242-244 (1957).

26. R. W. Redington, "Maximum Performance of High-Resistivity Photoconductors," J. Appl. Phys. **29**, 189-193 (1958).

27. P. K. Weimer, S. V. Forgue, and R. R. Goodrich, "The Vidicon—Photoconductive Camera Tube," RCA Rev. **12**, 306-313 (1951).

28. N. F. Mott and R. W. Gurney, *Electronic Processes in Ionic Crystals* (Clarendon Press, Oxford, 1948), pp. 168-173.

29. M. H. Crowell and E. F. Labuda, "The Silicon Diode Array Camera Tube," B.S.T.J. **48**, 1481-1528 (1969).

30. W. C. Dash and R. Newman, "Intrinsic Optical Absorption in Single-Crystal Germanium and Silicon at 77°K and 300°K," Phys. Rev. **99**, 1151 (1955).

☆ U.S. GOVERNMENT PRINTING OFFICE: 1976—777-018/25